Broadening of divertor heat flux profile with increasing number of ELM filaments in NSTX

# Letter

# Broadening of divertor heat flux profile with increasing number of ELM filaments in NSTX

**J.-W. Ahn**[1]**, R. Maingi**[2]**, J.M. Canik**[1]**, K.F. Gan**[3]**, T.K. Gray**[1] **and A.G. McLean**[4]

[1] Oak Ridge National Laboratory, Oak Ridge, TN, USA

[2] Princeton Plasma Physics Laboratory, Princeton, NJ, USA

[3] Institute of Plasma Physics, Chinese Academy of Science, Hefei, People's Republic of China

[4] Lawrence Livermore National Laboratory, Livermore, CA, USA

E-mail: jahn@pppl.gov

## Abstract

Edge localized modes (ELMs) represent a challenge to future fusion devices, owing to cyclical high peak heat fluxes on divertor plasma facing surfaces. One ameliorating factor has been that the heat flux characteristic profile width has been observed to broaden with the size of the ELM, as compared with the inter-ELM heat flux profile. In contrast, the heat flux profile has been observed to narrow during ELMs under certain conditions in NSTX. Here we show that the ELM heat flux profile width increases with the number of filamentary striations observed, i.e. profile narrowing is observed with zero or very few striations. Because NSTX often lies on the long wavelength current-driven mode side of ideal MHD instabilities, few filamentary structures can be expected under many conditions. ITER is also projected to lie on the current driven low-$n$ stability boundary, and therefore detailed projections of the unstable modes expected in ITER and the heat flux driven in ensuing filamentary structures is needed.

Keywords: ELM filament, divertor heat flux, NSTX

(Some figures may appear in colour only in the online journal)

## 1. Introduction

Fusion devices must exhaust both particles and heat from the main plasma. Steady state heat removal techniques for solid plasma facing components can remove up to $\sim 10\,\mathrm{MW\,m^{-2}}$, depending on the allowed transient heat fluxes [1]. One of the biggest threats to tokamaks in this regard is from repetitive heat and particle expulsion events common in high performance scenarios, termed edge localized modes (ELMs) [2]. In addition to thermal cycling and fatigue issues arising from thousands of ELMs, sufficiently large individual ELMs could lead to localized melting and re-freezing of surfaces, substantially altering thermal properties. Ejection of ablated material into the main plasma could even trigger disruptions. Thus characterization and understanding of the heat flux profiles is needed for projection of acceptable operational scenarios in future devices, e.g. ITER [3].

In an ELM, a fraction of the energy in the edge of the main plasma is expelled into the scrape-off layer (SOL), the region between the main plasma and walls, and it flows along open magnetic field lines to the divertor target. The magnitude of the edge plasma stored energy expulsion depends on the predominant instability and the physical process of ELM energy loss. In ITER, the fraction for a large ELM is expected to reach 5–10% if the SOL ion flow parallel time controls the energy loss and 15–20% if the edge plasma collisionality controls it [4], on time scales $\sim$ several hundred microseconds. The resulting transient heat fluxes to the divertor target can be $\sim 10$ times higher than the steady state heat fluxes [5, 6].

Many studies have identified that the onset of large ELMs, i.e. 'type I' ELMs, is correlated with the violation of ideal magnetohydrodynamic (MHD) stability limits, driven by current driven (kink/peeling), pressure driven (ballooning), or combined peeling–ballooning modes [7, 8]. Ballooning modes are short wavelength modes with high toroidal mode number $n > 20$. Kink/peeling modes are long wavelength modes with toroidal mode numbers $n < 5$. Coupled peeling–ballooning modes are often the most unstable, with $n \sim 10$–20,

for many tokamaks. Calculations have shown that the coupled peeling–ballooning modes naturally form 10–20 filamentary structures that propagate into the SOL and divertor [9–11]. Each of these filaments carries particles and energy [12]. The presence of these non-axisymmetric filaments of peeling–ballooning ELMs on top of the natural heat transport in the SOL and divertor has led to the general observation that the heat flux 'footprint' characteristic widths usually increase during ELMs, as compared to the footprint between ELMs, by factors of 2–5 [13]. Furthermore, several devices, e.g. JET and ASDEX-U, reported ELM heat flux profile broadening that increased with the size of the stored energy ejection during the ELM [13, 14]. Such a broadening would increase the size of tolerable ELMs in future devices, e.g. ITER [3], despite recent studies that have demonstrated that the inter-ELM heat flux footprints will be narrower than previously believed [15].

In contrast, narrowing of the heat flux footprint during large ELMs has been observed in NSTX. In other words, not only did the footprint *not* increase by several factors, but rather it *contracted* by up to 50%, exacerbating the heat flux challenge. In this paper, we present analysis showing that profile broadness is directly correlated with the number of filamentary striations measured in the ELM heat flux profile, i.e. profile narrowing is observed when very few or no striations are observed in the heat flux. We argue that this is related to the underlying instabilities that drive ELMs in NSTX, which are long wavelength current-driven modes of low toroidal mode number [16, 17] that are expected to lead to very few ejected filaments and resulting striations.

We note here that while ITER is also pursuing ELM suppression via Resonant Magnetic Perturbations pioneered by DIII-D [18, 19], physics interpretations from different devices [20–22] meet challenges due to different experimental conditions and varying plasma parameters. Thus ITER is also pursuing ELM mitigation via pellet injection, i.e. triggering of rapid, small ELMs to prevent the onset of a large ELM [23, 24]; hence, the ELM heat flux deposition dynamics are critical areas of current international fusion research. The implications of our results for ITER are discussed in the concluding paragraph.

## 2. Measurement and data analysis techniques

NSTX is equipped with a high speed infrared (IR) camera to monitor surface temperature with spatial resolution of ∼6 mm and frame rate up to 6.3 kHz [25]. At the fastest frame rates, the camera can usually provide 2–3 data points during the ELM rise phase, which was the case for almost all data points presented in this paper. The temporal array of measured 2D surface temperature is used in a 3D heat conduction solver, TACO, to produce 2D heat flux profiles. The original version of TACO has been improved to address the effect of surface layer (in the form of thin layer of damaged bulk material by impinging plasma particles or thin hydrocarbon composite layer from the interaction of carbon tile with the plasma) on the tile [26], similar to the method implemented in the widely used THEODOR code [27]. This technique is basically to treat the surface layer as a thin layer with no heat capacity. Then heat fluxes at the surface layer and at the surface of bulk material underneath are the same, and

the temperature difference between the layer and bulk is assumed to be proportional to the incident heat flux divided by a surface heat transmission coefficient, $\alpha = \kappa/d$ ($\kappa$ is the heat conductivity and $d$ is the thickness of the surface layer). By using an appropriate $\alpha$ value (without knowing $\kappa$ and $d$), this procedure is equivalent to the estimation of bulk temperature ($T_{\mathrm{bulk}}$) from the surface temperature ($T_{\mathrm{surf}}$) derived from the measured surface IR emission. For completeness, we note that the heat transmission coefficient of the layer, $\alpha$, introduced in the solution of heat conduction equation was set at 30–60 kW m$^{-2}$ K$^{-1}$ in this study, based on analysis of power balance [26]. Readers interested in this subject are encouraged to refer to [26] and [27] as well as other references therein. The calculated 2D heat flux profiles are re-mapped from the $(x, y)$ Cartesian field of view plane to the physical $(r, \Phi)$ plane, which enables clearer visualization of the toroidal and radial structure of the ELM heat deposition.

Figure 1 illustrates the three steps of this procedure described above. Figures 1(a) and (b) shows the measured 2D surface temperature and the calculated heat flux profile in the $(x, y)$ plane, respectively, for an inter-ELM time slice. The peak heat flux can be seen along the strike point (where the magnetic separatrix intersects with the tile surface) in the toroidal direction in figure 1(c). 1D radial heat flux profiles taken at multiple toroidal locations are averaged to produce a mean radial profile, $\bar{q}(r)$, for the data analysis. This represents the entire 2D heat flux data observed by the IR camera. Figure 2 illustrates a mean 1D radial profile at a specific time slice, obtained through this procedure. It can be seen that the profile peaks at the radius of 0.36 m ($r_{\mathrm{peak}}$) with a magnitude of 2 MW m$^{-2}$ ($q_{\mathrm{peak}}$).

Now we define a number of terms that will be presented in the analysis and discussion, also shown in figure 2. The total deposited power to the divertor surface is obtained by integrating the mean heat flux in both the radial and toroidal directions: $P_{\mathrm{div,IR}} = \int 2\pi r \bar{q}(r)\,\mathrm{d}r$; this equation assumes toroidal symmetry. The characteristic area onto which the total power is deposited is defined as the 'wetted area': $A_{\mathrm{wet}} = P_{\mathrm{div,IR}}/q_{\mathrm{peak}}$. Because $q_{\mathrm{peak}}$ determines the peak surface temperature ($T_{\mathrm{peak}}$), which must be maintained below the melting limit, increasing $A_{\mathrm{wet}}$ is necessary to keep $q_{\mathrm{peak}}$ as low as possible. Additionally, a characteristic length in the radial direction that represents how wide the heat flux profile is, i.e. integral heat flux width, can be defined: $\lambda_q = P_{\mathrm{div,IR}}/2\pi r_{\mathrm{peak}} q_{\mathrm{peak}} = A_{\mathrm{wet}}/2\pi r_{\mathrm{peak}}$. Finally the total deposited energy to the divertor surface is obtained from the heat flux data by time integrating deposited power: $W_{\mathrm{div,IR}} = \int P_{\mathrm{div,IR}}\,\mathrm{d}t$. Temporal evolution of these parameters, particularly $P_{\mathrm{div,IR}}$ and $A_{\mathrm{wet}}$, during the ELMs will be presented and the relation with ELM filaments will be discussed in the remainder of this paper.

Plasma discharges studied in this work had the following operating parameters: plasma current $0.7 \leqslant I_{\mathrm{p}} \leqslant 1.2$ MA, toroidal field $0.4 \leqslant B_{\mathrm{t}} \leqslant 0.5$ T, and NBI heating power $4 \leqslant P_{\mathrm{NBI}} \leqslant 6$ MW. Type I ELMs were primarily investigated, with up to ∼14% loss of total stored energy ($\Delta W_{\mathrm{MHD}}/W_{\mathrm{MHD}}$), and data for a total of 62 ELMs are presented in this paper. All discharges were lower single null (LSN) configuration and heat flux data in this work are all for outer lower divertor.
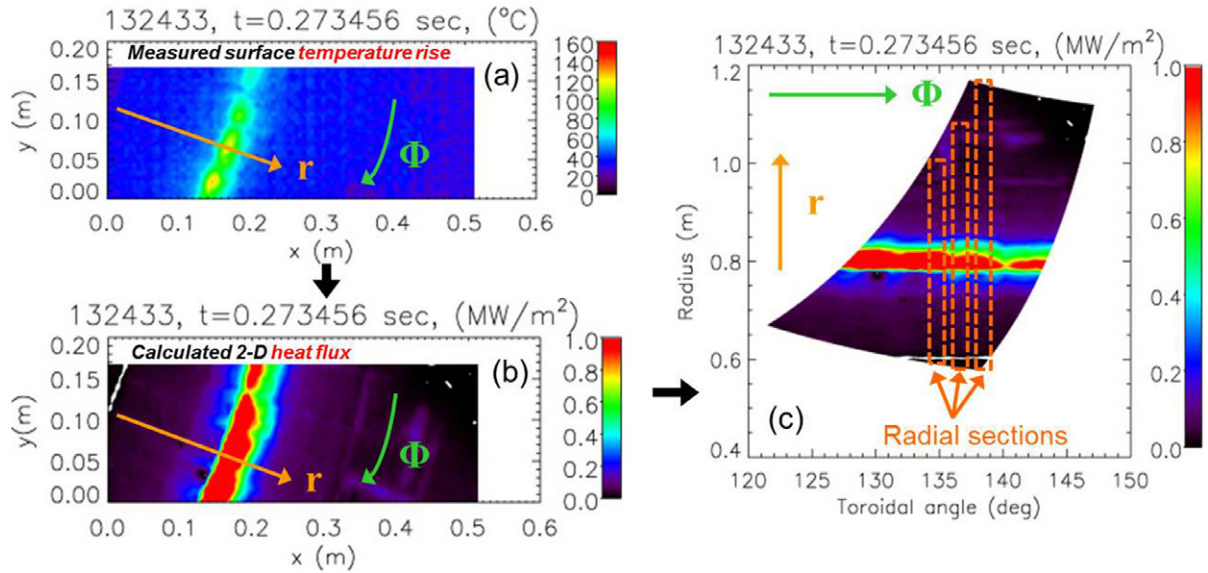
**Figure 1.** (*a*) Measured surface temperature of outer-lower divertor by the IR camera during an inter-ELM period in NSTX, (*b*) calculated 2D heat flux profile from TACO using the surface temperature data, and (*c*) the re-mapped heat flux data from the (*x*, *y*) to the (*r*, $\Phi$) plane.
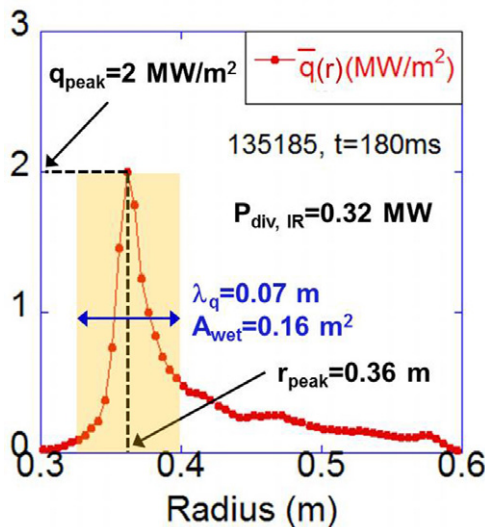


**Figure 2.** An example of mean 1D radial heat flux profile during an inter-ELM period, averaged over multiple profiles at different toroidal locations, see figure 1(*c*).

## 3. Dynamics of heat flux deposition with varying number of ELM filaments

The impact of striations on the 2D and 1D radial heat flux profiles during ELMs is shown in figure 3. Both profiles in figures 3(*a*) and (*b*) were taken at ELM peak times. The number of striations caused by an ELM can be simply counted by comparing both 1D and 2D data during the ELM to those before the ELM. Figure 3(*a*) is for an ELM with no striations observed other than the peak heat flux at the strike point, while figure 3(*b*) shows four or five striations caused by ELM filaments. It is clear even from these data that the footprint broadens with the number of striations.

Temporal evolution of $A_{wet}$, $P_{div,IR}$ and $q_{peak}$ across an ELM are shown in figure 4 for the case of no striation

(figure 4(*a*)) and multiple striations (figure 4(*c*)). Radial profiles for each case are also shown in figures 4(*b*) and (*d*), colour coded for three stages: beginning of ELM, during the ELM rise phase, and at the ELM peak time. IR camera integration time for each frame is indicated as a brown bar in the top figure, which is 32 $\mu$s out of 160 $\mu$s of frame time for figure 4(*a*), for a period of 832 $\mu$s near the ELM rise phase. The integration time is adjustable and was in the range 16–32 $\mu$s for the dataset presented in this paper, depending on the choice for specific discharges to take a balance between high enough signal-to-noise ratio (SNR) and the need to avoid signal saturation during the ELM. It can be seen in figures 4(*a*) and (*b*) that the ELM reduces $A_{wet}$ by 40–50% when there are no striations observed (compare red, $t = 273.456$ ms, and green, $t = 273.774$ ms). This reduction in $A_{wet}$ raised $q_{peak}$ by more than a factor of 3, even though the total power during the ELM increased only by a factor of $\sim$2. On the other hand, the ELM in figures 4(*c*) and (*d*) resulted in multiple observable striations. Compared to the profile immediately before the ELM ($t = 472.332$ ms, red), the profile during the ELM at $t = 473.160$ ms (blue) shows 3–4 striations for $r > 0.5$ m. The $A_{wet}$ change at the respective times shows slight reduction and $q_{peak}$ increases accordingly. However, the profile shows 8–9 striations at the next time slice ($t = 473.367$ ms, green) and this reduces $q_{peak}$ even though the total power during the ELM continues to increase. These data further corroborate the inference that $A_{wet}$ contraction or expansion correlates with number of striations.

ELM dynamics exhibit moderate variability during ELMs and across multiple ELMs. The ELM heat flux can evolve in such a way that both $A_{wet}$ expansion and contraction can be observed during the evolution of a single ELM. An example of this behaviour is shown in figure 5. The profile shows no striation before the ELM begins. During the ELM rise phase 3–4 striations ($t = 245.204$ ms, blue) appear, which slightly increases $A_{wet}$, unlike the slight reduction of $A_{wet}$ seen in figure 4(*c*) and (*d*). However, at the next
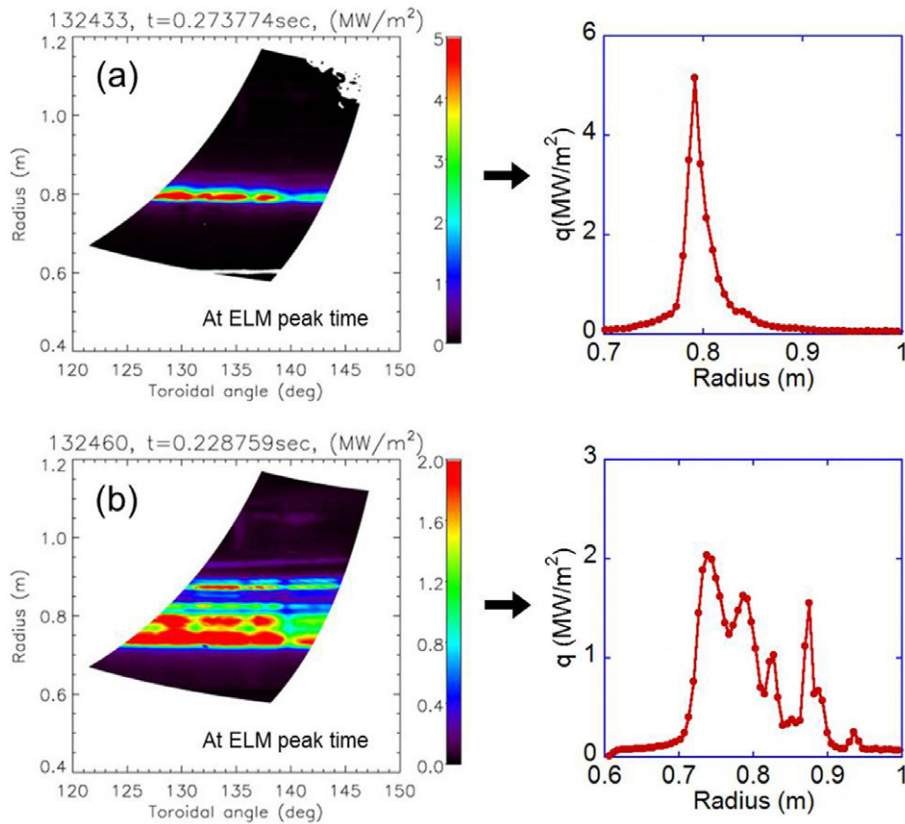
**Figure 3.** Example of 2D divertor heat flux profiles (left plots), along with the mean 1D radial profiles (right) at ELM peak times. (*a*) is for an ELM with no striation except that for strike point and (*b*) is for an ELM with ~5 additional striations.

time slice corresponding to the ELM peak heat flux time (t = 245.363 ms, green), the striations disappear and the profile becomes more peaked. This reduces $A_{wet}$ and rapidly increases $q_{peak}$, although the total power increase during the ELM is somewhat modest.

The observations in figures 4 and 5 illustrate that $A_{wet}$ decreases (i.e. the profile contracts) when the number of striations is less than 3–4, and increases (profile broadening) when more than 3–4. Figure 6 is a summary of $A_{wet}$ change as a function of the number of striations observed in the profile for a number of ELMs. Each data point was taken at the ELM peak time, and there are two groups of data shown in the figure. The red points represent ELMs with 0–4 striations, from discharges of weaker shaping ($\kappa \sim 1.9$, $\delta \sim 0.5$), which show profile contraction, i.e. $\Delta A_{wet} < 0$, for most of the data. The blue points are for ELMs with 2–9, from discharges of stronger shaping ($\kappa \sim 2.5$, $\delta \sim 0.75$), and indicate the profiles broadened, i.e. $\Delta A_{wet} > 0$, for many of the data points. We suspect that stronger shaping should have moved the operating point from the peeling boundary towards the peeling–ballooning boundary, which features higher $n$-number and therefore more number of ELM filaments. It is clear from the combined dataset that the 3–4 striations represent the threshold between heat flux profile contraction or expansion. Detailed study of the impact of shape parameters as well as pedestal collisionality on the ELM behaviour will be conducted in the future when NSTX-Upgrade is complete and the experiment resumes.

## 4. Discussion and conclusions

The striations in the heat flux profile logically represent ELM filaments, and therefore are related to the toroidal mode number of ELMs before expulsion of the filaments during the non-linear evolution of the ELM [9]. We note a couple of caveats with this statement. First, non-linear interaction between higher-$n$ modes can lead to beat frequencies, coalescing into single dominant filamentary structures, as reported in numerical studies [28]. This would tend to narrow measured ELM heat flux profiles. Second, the primary filaments from ELMs can sometime spawn multiple secondary, turbulent-like filaments [29, 30]. These would tend to broaden the measured heat flux profile, but could be separated during temporal evolution of ELMs for thermography systems with sufficient time resolution. The NSTX thermography system would be unable to resolve these effects; nonetheless, other NSTX studies have identified ELM evolution in soft x-ray light, i.e. in the vicinity of the H-mode pedestal from which ELMs originate, as low-$n$ modes [31, 32]. Assuming that the IR camera view covers sufficient radial range for all ELM filaments to be captured, we therefore submit that the striation data of NSTX reported in this paper is well correlated with the ELM filaments. Moreover, we confirmed from a wide angle visible camera data that covers almost full toroidal and radial range of the lower divertor [33] that some ELM filaments occur more than once at different radial locations at a single time slice. This is because an ELM filament appears to follow
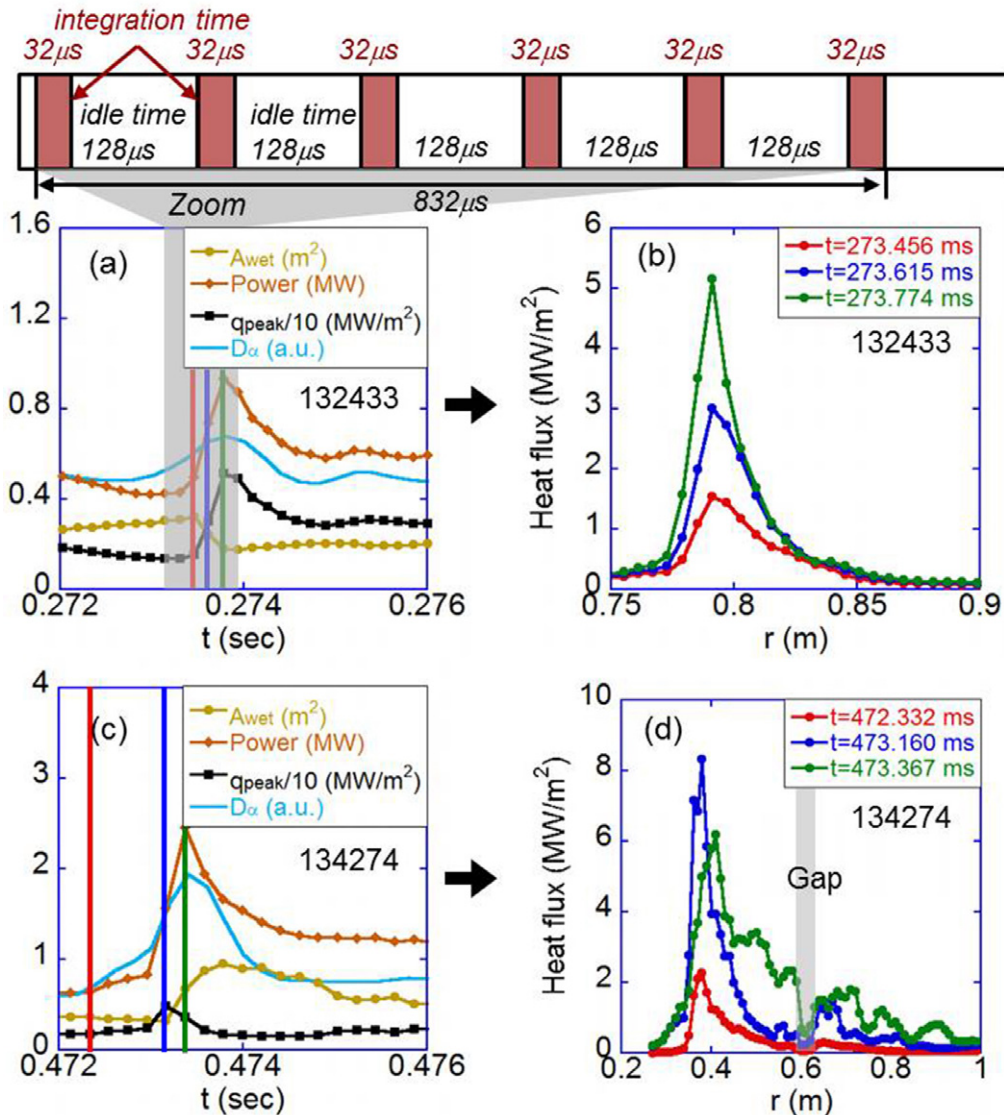
**Figure 4.** Temporal evolution of $A_{wet}$, $P_{div,IR}$, $q_{peak}$ and divertor $D_\alpha$ (left column) and 1D radial heat flux profiles (right column) across an ELM. Heat flux profiles are colour coded for specific time slices indicated by the vertical lines in the left plots. (*a*) and (*b*) are for an ELM with no striation by the ELM, and (*c*) and (*d*) are for an ELM with 8–9 striations. The dip in the 1D profiles at $r \sim 0.6$ m in (*d*) is due to the gap between tiles, indicated by the grey vertical bar. IR camera integration time for each frame is indicated as a brown bar in the top figure ($32\,\mu$s out of $160\,\mu$s of frame time for shot 132433, figure 4(*a*)).

the field line and helically deposits heat and particle flux to the divertor surface, and therefore a single striation can revolve toroidally more than once. This indicates that the toroidal mode number of ELM filaments can be even smaller than the counted number of striations from the camera data, which is consistent with the quoted *n*-number of ELMs in NSTX ($n = 1$–5) [16, 17] and the number of observed striations (0–10) from the IR data reported in this work. Hence it follows from the data in this paper that low-*n* modes are tied to fewer ELM heat flux striations, which can lead to a reduction in $A_{wet}$ during ELMs, further exacerbating peak heat fluxes. Data shown in this paper demonstrate that heat flux carried by ELM filaments tends to be more concentrated near the strike point when there are only a few filaments, leading to a more peaked heat flux profile and therefore to a smaller $A_{wet}$, while more filaments tend to spread heat over a wider area, i.e. a larger $A_{wet}$. Also, we observe that the total power estimated from the

IR measurement, which represents the ELM size, increases with increasing number of striations. This is consistent with the conjecture in a previous study [34] that ELMs with larger energies distribute their energy on average onto a larger number of striations.

For ITER, the pedestal pressure gradient and characteristic width predicted by the EPED model [35] has been used to generate model kinetic equilibria. Stability analysis of these equilibria showed that low-*n* kink/peeling modes are predicted to have the highest growth rates [36]. In other words, the situation in ITER could very well reflect the NSTX observations presented in this paper, that $A_{wet}$ might be reduced during ELM for sufficiently low toroidal mode number. For example, ITER will have plasma shape with $\kappa (= 1.85)$ and $\delta (= 0.48)$ very similar to the value of NSTX with 'weaker' shaping presented in this paper, which produced ELMs with small number of filament striations (0–4), although pedestal
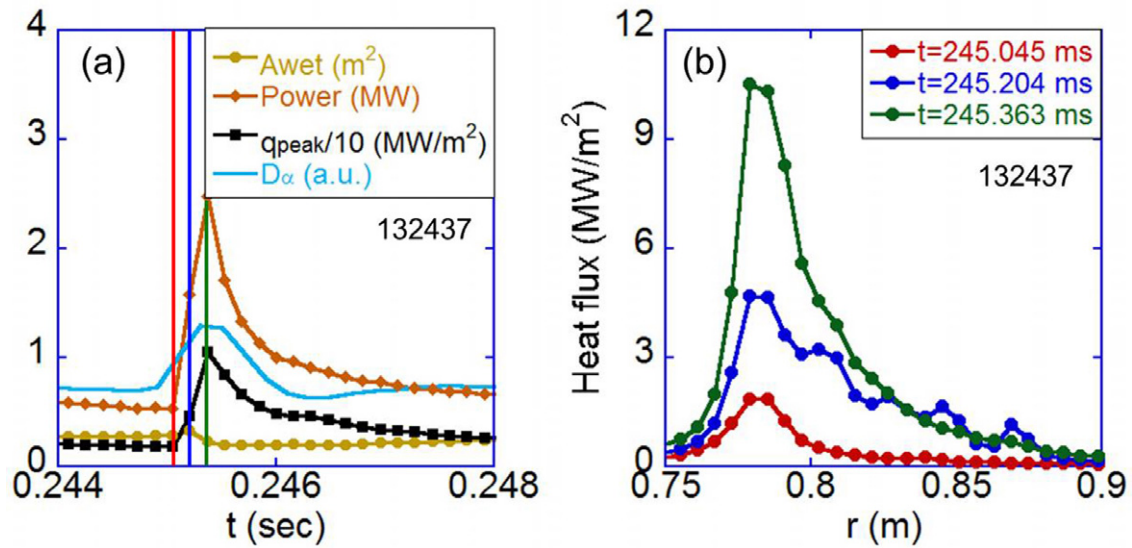
**Figure 5.** (*a*) Temporal evolution of $A_{wet}$, $P_{div,IR}$, $q_{peak}$ and divertor $D_\alpha$, and (*b*) 1D radial heat flux profiles, for an ELM with ∼3 striations in the middle of ELM rise phase and no striation at the ELM peak time. Heat flux profiles are colour coded for specific time slices indicated by the vertical lines in the left plot.
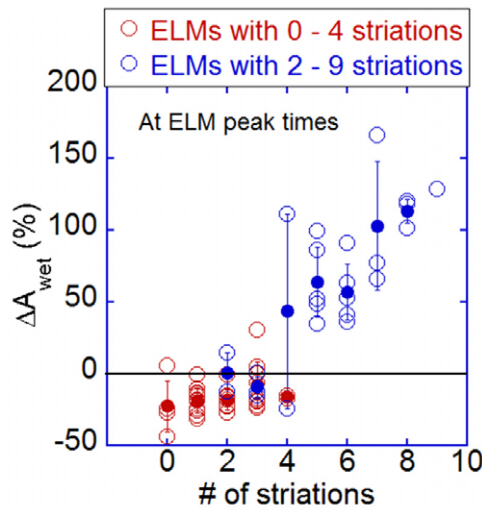


**Figure 6.** Change of wetted area by ELMs with respect to the value immediately before each ELM, as a function of the number of striations observed in the heat flux profiles. There are two groups of data overlaid in this plot; the red points represent ELMs with 0–4 striations and the blue points are for ELMs with 2–9 striations. The two groups of data points are from discharges with two different groups of shape parameters (see text). Open circles represent individual data points and solid circles are the average value of relative $A_{wet}$ change for each striation number. Error bars indicate standard deviation.

collisionality is another important parameter to affect ELM stability regime ($\nu^*_{e,ped} < 0.1$ for ITER versus $\nu^*_{e,ped} > 1$ for NSTX). Thus, a detailed study over a range of density and temperature profiles projected from transport analysis for ITER is advocated, to determine edge stability maps. In particular, identification of scenarios that move the ITER projected operating points up to higher-*n* stability limits would reduce the risk of extra, presently unaccounted peaking of the heat flux profile during ELMs.

## Reference

[1] Federici G. *et al* 2001 *Nucl. Fusion* **41** 1967
[2] Zohm H. 1996 *Plasma Phys. Control. Fusion* **38** 105
[3] Loarte A. *et al* 2014 *Nucl. Fusion* **54** 033007
[4] Loarte A. *et al* 2003 *Plasma Phys. Control. Fusion* **45** 1549
[5] Hill D.N. *et al* 1997 *J. Nucl. Mater.* **241–243** 182
[6] Eich T. *et al* 2003 *J. Nucl. Mater.* **313–316** 919
[7] Snyder P.B. *et al* 2002 *Phys. Plasmas* **9** 2037
[8] Wilson H.R. *et al* 2006 *Plasma Phys. Control. Fusion* **48** A 71
[9] Wilson H.R. and Cowley S.C. 2004 *Phys. Rev. Lett.* **92** 175006
[10] Kirk A. *et al* 2004 *Phys. Rev. Lett.* **92** 245002
[11] Kirk A. *et al* 2006 *Phys. Rev. Lett.* **96** 185001
[12] Eich T. *et al* 2003 *Phys. Rev. Lett.* **91** 195003
[13] Eich T. *et al* 2001 *J. Nucl. Mater.* **415** S856
[14] Devaux S. *et al* 2011 *J. Nucl. Mater.* **415** S865
[15] Eich T. *et al* 2011 *Phys. Rev. Lett.* **107** 215001
[16] Maingi R. *et al* 2009 *Phys. Rev. Lett.* **103** 075001
[17] Boyle D.P. *et al* 2011 *Plasma Phys. Control. Fusion* **53** 105011
[18] Evans T.E. *et al* 2004 *Phys. Rev. Lett.* **92** 235003
[19] Evans T.E. *et al* 2006 *Nature Phys.* **2** 419
[20] Liang Y. *et al* 2007 *Phys. Rev. Lett.* **98** 265004
[21] Suttrop W. *et al* 2011 *Phys. Rev. Lett.* **106** 225004
[22] Jeon Y.M. *et al* 2012 *Phys. Rev. Lett.* **109** 035004
[23] Baylor L.R. *et al* 2013 *Phys. Rev. Lett.* **110** 245001
[24] Lang P.T. *et al* 2013 *Nucl. Fusion* **53** 043004
[25] Ahn J.-W. *et al* 2010 *Rev. Sci. Instrum.* **81** 023501

[26] Gan K.F. *et al* 2013 *Rev. Sci. Instrum.* **84** 023505
[27] Herrmann A. *et al* 2001 *Proc. 28th EPS Conf. on Controlled Fusion and Plasma Physics (Madeira, Portugal, 2001)* www.cfn.ist.utl.pt/EPS2001/CD/pdfs/P5.104.pdf
[28] Snyder P.B. *et al* 2005 *Phys. Plasmas* **12** 056115
[29] Maqueda R.J. *et al* 2009 *Phys. Plasmas* **16** 056117
[30] Maqueda R.J. *et al* 2009 *J. Nucl. Mater.* **390–391** 843

[31] Maingi R. *et al* 2005 *Nucl. Fusion* **45** 1066
[32] Maingi R. *et al* 2006 *Phys. Plasmas* **13** 092510
[33] Scotti F. *et al* 2012 *Rev. Sci. Instrum.* **83** 10E532
[34] Eich T. *et al* 2005 *Plasma Phys. Control. Fusion* **47** 815
[35] Snyder P.B. *et al* 2009 *Nucl. Fusion* **49** 085035
[36] Snyder P.B. *et al* 2011 *Nucl. Fusion* **51** 103016